

**Superhydrophobic surfaces to reduce form drag in turbulent separated flows**J.-P. Mollicone,<sup>1</sup> F. Battista,<sup>2</sup> P. Gualtieri,<sup>2</sup> and C.M. Casciola<sup>2</sup><sup>1</sup>*Department of Mechanical Engineering, Faculty of Engineering, University of Malta, MSD 2080, Msida, Malta<sup>a)</sup>*<sup>2</sup>*Department of Mechanical and Aerospace Engineering, Sapienza University of Rome, via Eudossiana 18, 00184, Rome, Italy*

(Dated: May 10, 2022)

The drag force acting on a body moving in a fluid has two components, friction drag due to fluid viscosity and form drag due to flow separation behind the body. When present, form drag is usually the most significant between the two and in many applications, streamlining efficiently reduces or prevents flow separation. As studied here, when the operating fluid is water, a promising technique for form drag reduction is to modify the walls of the body with superhydrophobic surfaces. These surfaces entrap gas bubbles in their asperities, avoiding the direct contact of the liquid with the wall. Superhydrophobic surfaces have been vastly studied for reducing friction drag. We show they are also effective in reducing flow separation in turbulent flow and therefore in reducing the form drag. Their conceptual effectiveness is demonstrated by studying numerical simulations of turbulent flow over a bluff body, represented by a bump inside a channel, which is modified with different superhydrophobic surfaces. The approach shown here contributes to new and powerful techniques for drag reduction on bluff bodies.

---

<sup>a)</sup>jean-paul.mollicone@um.edu.mt

## I. INTRODUCTION

One of the current global challenges is to reduce the amount of energy used for human activities in order to preserve natural resources and safeguard the environment. A considerable amount of energy is used to overcome drag forces and much effort is dedicated to efficient control and reduction drag. Two drag sources exist in a turbulent flow over a bluff, non-lifting body moving in an incompressible fluid (note: for lifting bodies the induced drag needs to be taken into account, while wave drag concurs in compressible and in free-surface flows in presence of gravity). The two sources of drag are: friction at the wall associated with fluid viscosity (friction drag) and lack of pressure recovery behind the body associated with flow separation (form drag)<sup>1</sup>.

When present, flow separation prevails, since friction drag is subdominant at large speed. In such conditions, the traditional approach to drag control still mostly relies on body streamlining, i.e. body shape optimisation aimed at preventing/limiting flow separation. The drag force  $D$  is expressed by the drag coefficient,  $C_D = D/(1/2\rho U_\infty^2 L^2)$ , in terms of fluid density  $\rho$ , free stream velocity  $U_\infty$  and body frontal section area  $A \sim L^2$ ,  $L$  being the body characteristic length scale. While the friction drag coefficient decreases with the Reynolds number,  $Re = \rho U_\infty L/\mu$  ( $\mu$  is the dynamic fluid viscosity), scaling as a power law with negative exponent ( $\alpha = -1/2$  for laminar cases and  $\alpha \approx -1/5$  for turbulent cases), the form drag coefficient is Reynolds independent at high enough Reynolds numbers<sup>2</sup>, being connected to the phenomenon of “dissipative anomaly” in turbulence<sup>3</sup>. It is therefore wise to target the form drag in all cases where flow separation cannot be avoided by simple streamlining.

Reducing form drag is a challenging problem in both fundamental and applied fluid dynamics. Several solutions have been proposed, with both active devices (e.g. blow/suction<sup>4,5</sup>, gas injection<sup>6</sup>) and passive devices (e.g. Large-Eddy Breakup Devices<sup>7</sup> and riblets<sup>8,9</sup>). The drawback of active techniques is the energy necessary to actuate the control mechanisms and the complexity of the actuator system. On the other hand, passive devices lose their effectiveness in off-design conditions.

A richer set of possibilities are available for friction drag control. Among these, relevant for our present purposes, are passive techniques based on superhydrophobic surfaces (SHSs)<sup>10,11</sup> and on liquid impregnated surfaces<sup>12</sup>. Their application, though limited to applications in water, shows encouraging results in friction drag reduction<sup>13–17</sup> in both laminar<sup>18,19</sup> and turbulent regimes<sup>20,21</sup> and have been studied in a variety of domains such as, for example, channels<sup>22</sup>, Taylor-Couette flow<sup>23</sup>, pipe flow<sup>24</sup> and around rotors<sup>25</sup>. Inspired by nature<sup>26</sup>, SHSs trap gas bubbles in their asperities, allowing liquid moving onto the gaseous phase to slip, unlike at solid walls where the liquid adheres<sup>27–32</sup>.

The simulations discussed in the present paper suggest that SHSs can also be effective in reducing form drag of bluff bodies in turbulent flow. Turbulence models cannot reliably predict the flow behaviour outside the range of conditions for which the model has been developed and tested. Since this is the case of SHSs, the full Navier-Stokes equations are solved on a supercomputer by the Direct Numerical Simulation (DNS) approach<sup>33</sup>, which resolves all the relevant physical scales of the flow (no turbulence models).

The configuration addressed here follows from a compromise between fidelity to the actual conditions and numerical efficiency. The geometry consists of a bump (or bulge, representing the bluff body) mounted on one of the two otherwise planar and parallel surfaces bounding a

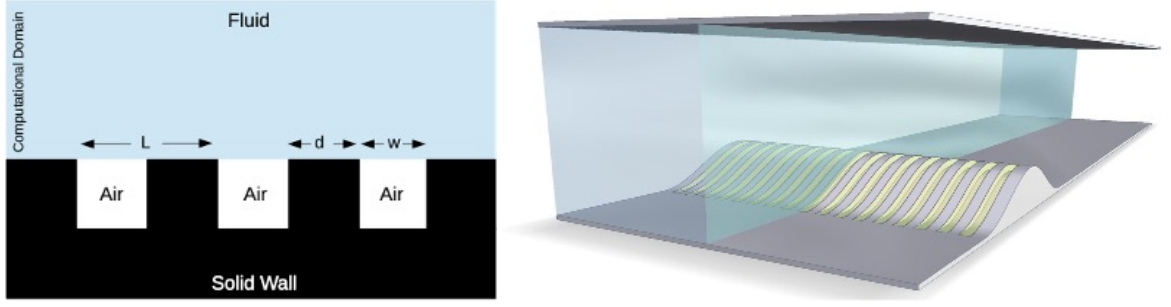


Figure 1. The superhydrophobic surface made by alternating stripes and grooves (left panel), is reproduced in numerical simulations by no-slip (gray) and free-shear (yellow) patterns (right panel).

channel of height  $2h$ . The bump, of characteristic length  $2h$ , features a system of SHSs with the purpose to investigate their effect on the flow separation occurring behind the obstacle and the related form drag. In absence of SHSs, the bump is known to make the flow separate, creating a strong shear layer emanating from the separation point and producing a recirculating region<sup>34–36</sup>. The configuration, with no SHSs has been extensively investigated using classical statistical tools of turbulence theory<sup>37–42</sup>.

## II. CASE SETUP

Direct Numerical Simulations (DNSs) of turbulent channel flow containing a bump at one of the walls are performed by solving the incompressible Navier-Stokes equations,

$$\nabla \cdot \vec{u} = 0 \quad (1)$$

$$\frac{\partial \vec{u}}{\partial t} + \nabla \cdot \vec{u} \otimes \vec{u} = -\nabla p + \nu \nabla^2 \vec{u} + \vec{f} \quad (2)$$

where  $t$  is the time,  $\vec{u}$  is the fluid velocity vector,  $p$  is the hydrodynamic pressure,  $\nu$  is the kinematic viscosity and  $\vec{f} = \Delta p / L_x \hat{e}_x$  is the constant pressure gradient that sustains the flow rate inside the channel, ( $\hat{e}_x$  is the unit vector in the streamwise direction). The solver used is Nek5000<sup>43</sup>, an open-source code based on the spectral element method (SEM)<sup>44</sup>. The SEM combines high accuracy of spectral methods and the flexibility, in terms of geometrical configuration, of finite element approaches. The computational domain has dimensions  $[L_x \times L_y \times L_z] = [20 \times 2 \times 2\pi] \times h$ , where  $x$ ,  $y$ , and  $z$  are the streamwise, wall-normal and span-wise coordinates respectively and  $h$  is the nominal half channel height. All quantities are made dimensionless with respect to the bulk velocity  $U_b = Q/(2h)$ , where  $Q$  is the flow rate per unit width. Flow is in the  $x$  direction with periodic boundary conditions in both  $x$  and  $z$  directions. The periodicity in the streamwise direction replicates a periodic array of bumps, similar to the experimental configuration found in<sup>40</sup>. The periodic configuration is instrumental in avoiding spurious effects that artificial inflow/outflow boundary conditions could induce and allows the analysis of an almost isolated bump, with definite flow reattachment and negligible streamwise correlation. The simulations are carried out at bulk Reynolds numbers  $Re = 5000$ . The maximum friction Reynolds number, achieved close to the bump tip for the reference simulation is  $Re_\tau = u_\tau h / \nu = 540$ , where  $u_\tau = \sqrt{\tau_w / \rho}$  is the local friction velocity and  $\tau_w$  is the shear stress at the wall. The friction

Table I. Simulation details: simulation name (first column), periodicity length of the no-slip/free-shear stripes normalised with half channel height (second column), periodicity length of the stripes normalised with the viscous length (third column), grid spacing normalised with the viscous length in streamwise (forth column), wall normal (fifth column) and spanwise (sixth column) directions, number of computational points in millions (seventh column). The two values in the fifth column refer to the grid spacing at the channel center (max) and at the wall (min).

Simulation	$L$	$L^+$	$\Delta x^+$	$\Delta y_{max/min}^+$	$\Delta z^+$	Grid points
REF	–	–	8.0	4/0.5	9.0	$101 \cdot 10^6$
L20	0.071	20	7.5	4/0.5	1.8	$544 \cdot 10^6$
L40	0.142	40	7.5	4/0.5	3.5	$274 \cdot 10^6$
L80	0.284	80	7.5	4/0.5	7.0	$138 \cdot 10^6$

velocity and the viscous length,  $y_\tau = \nu/u_\tau$ , which are the characteristic parameters in turbulent wall-bounded flows, are used as reference quantities to normalise the velocity and length scales, respectively, and are indicated with the  $^+$  superscript. To the best of our knowledge, the friction Reynolds number is the highest reached in the literature concerning DNS of similar geometries.

No-slip boundary conditions are enforced at the top and bottom walls except on the bump, where the superhydrophobic surface is modelled by alternating no-slip/shear-free boundary conditions, see figure 1. These boundary conditions mimic the presence of ridges of width  $d$  (solid wall) alternated with grooves of width  $w$ . Physically, gas is assumed to be stably trapped in the grooves, hence allowing the slippage of the liquid on top, corresponding to vanishing shear force,<sup>45</sup>. The pattern is aligned in the streamwise direction, see right panel of figure 1. A liquid-gas interface is pinned at the edge of the grooves, resembling a stable Cassie-Baxter state, as shown in the left panel of figure 1. The no-slip and the no-penetration boundary conditions are enforced on the ridge, being a solid wall, and the shear-free and the no-penetration boundary conditions are enforced on the liquid-gas interface. The interface is then a fixed boundary on which a perfect slip condition is applied. The groove width,  $w$ , is changed whilst the solid fraction, i.e. the solid surface to the overall surface ratio, is kept constant at  $\phi_S = 0.5$ , implying that  $d = w$ . The periodicity  $L$  therefore changes, since  $L = d + w$ .

Table I shows a summary of the simulation parameters. The first column lists the names of the simulations, where REF is the reference simulation with a fully no-slip bump wall condition and the superhydrophobic cases are labelled depending on the dimension of the grooves. The second column shows the periodicity length normalised with the half channel height whilst the third column lists the periodicity length normalised with the viscous length. The fourth, fifth and sixth columns provide the computational grid spacing normalised with the viscous length in streamwise, wall-normal and spanwise directions, respectively. The grid is uniform in the streamwise and spanwise directions and stretched along the wall normal direction to cluster grid nodes toward the walls. The number of nodes in the spanwise direction are increased with decreasing periodicity to obtain adequate grid resolution over the no-slip/shear-free boundary conditions on the bump. The seventh column lists the number of collocation points. The simulations have been carried out on supercomputing facilities. The high computational costs are due to the fine computational grids required to resolve the turbulent scales and the SHS pattern especially when the periodicity length is small. The statistics discussed are based on 300

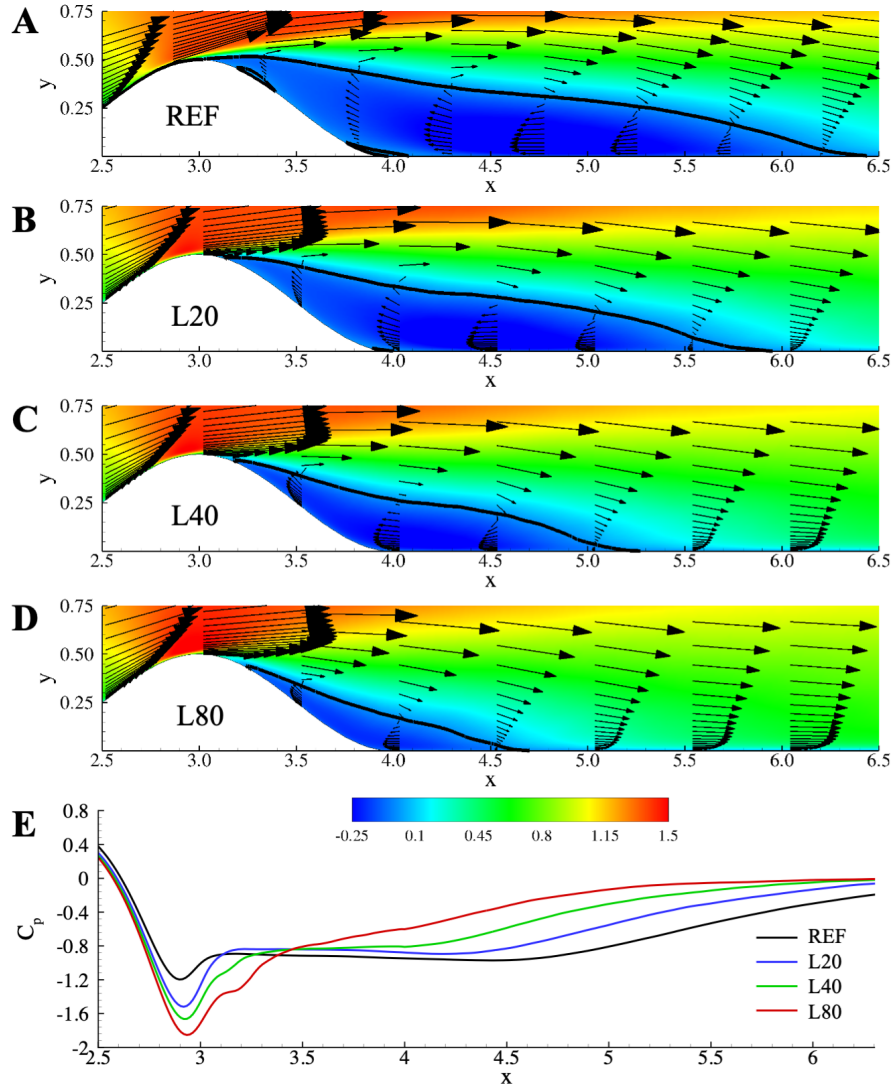


Figure 2. Coloured contour of mean streamwise velocity normalised with the bulk velocity and corresponding zero isoline (black solid line), in panels from A to D for simulations REF, L20, L40, and L80, respectively. Pressure coefficient along the bottom wall for all the simulations in panel E.

independent samples of the flow field collected at instants separated in time by more than the flow turnover time which largely exceeds the maximum correlation time of velocity and pressure fluctuations. Convergence is enhanced by exploiting the statistical spanwise homogeneity of the flow. The channel and bump dimensions and the Reynolds number are kept fixed and therefore the periodicity length is the control parameter of the system. Separation and reattachment points are evaluated by finding the streamwise position where the wall-normal derivative of the mean velocity parallel to the wall is zero. To evaluate the reattachment point, the velocity component parallel to the wall coincides with the streamwise velocity, whilst for the separation point, the mean velocity tangential to the bump is considered.

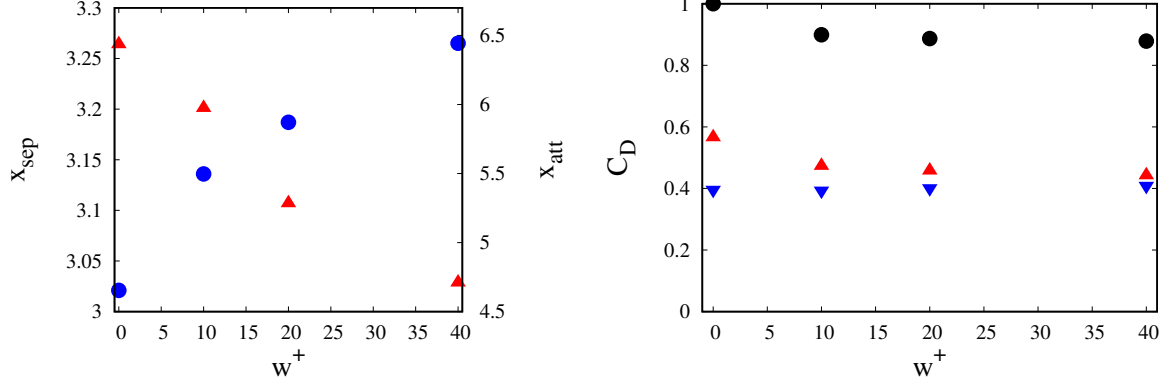


Figure 3. Left panel: plot of separation (blue circle ●) and reattachment points (red triangle ▲) against the groove width normalised with the viscous length. Right panel: plot of drag coefficient components; total (black circle ●), form (red triangle ▲) and friction (blue gradient ▼), against the groove width normalised with the viscous length.

### III. RESULTS

One of the two central results of this work is illustrated in figure 2, panels A to D. In the plots, the arrows reproduce the mean flow velocity averaged on 300 instantaneous flow fields sampled along the simulation and separated by the velocity autocorrelation time. The extension of the recirculation region behind the obstacle decreases with increasing the periodicity length  $L$  of the stripes at  $d/w = 1$ . The left panel in figure 3 shows that when the groove dimension increases, the separation point  $x_{sep}$  moves downstream and the reattachment point  $x_{att}$  upstream, resulting in a smaller separation bubble. The change in the mean velocity in figure 2 is accompanied by a change in the pressure distribution along the bump, which is reproduced in panel E. As expected, when reducing the size of the recirculating region, the pressure behind the obstacle increases, therefore the form drag decreases, see eq. (5).

The decrease in form drag is the second central result of the work and is shown in the right panel of figure 3, which concerns the drag exerted on the obstacle. The drag coefficient is defined as

$$C_d = -\frac{2}{L_x} \int_{walls} \langle \vec{t} \rangle \cdot \hat{e}_x dl, \quad (3)$$

while the friction and form drag coefficients are defined as

$$C_d^{form} = -\frac{2}{L_x} \hat{e}_x \cdot \int_{walls} P \vec{n} dl \quad (4)$$

$$C_d^{friction} = -\frac{2}{L_x} \hat{e}_x \cdot \int_{walls} \mu \frac{\partial \langle \vec{u}_{||} \rangle}{\partial \vec{n}} dl, \quad (5)$$

respectively.  $\vec{t}$  is the (dimensionless) traction at the wall and  $\hat{e}_x$  is the unit vector in the streamwise direction, the angular brackets define the ensemble average in time and spanwise direction,  $P$  is the average pressure,  $\vec{n}$  is the unit normal exiting the fluid domain, and the dot represents the scalar product. The total drag is reduced by up to 12% with respect to the reference case with no SHS, since the form drag is reduced by up to 22%.

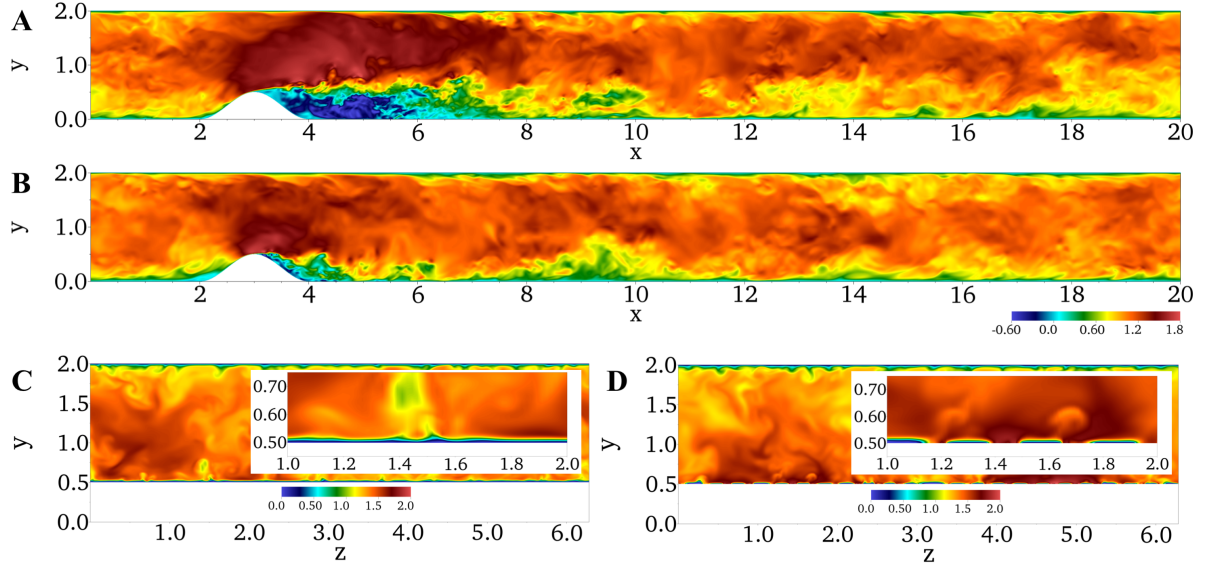


Figure 4. Instantaneous streamwise velocity, normalised with the bulk velocity, in  $x - y$  plane (panels A and B) and  $y - z$  plane at the top of the bump (panels C and D) concerning reference simulation (A and C) and simulation L80 (B and D); the insets in panel C and D report a detail of the wall, with the latter showing the superhydrophobic surface.

The decrease in recirculation bubble dimension is due to the increase in turbulent velocity fluctuations induced by the wall pattern. The wall pattern induces vortical structures that are anchored to the no-slip/shear-free interfaces and that transfer fluctuations on to the no-slip surface and away from the wall<sup>22,24,27</sup>. The increase in fluctuations promotes the delay of the separation point and consequently an earlier reattachment of the flow, resulting in a sensible decrease of the form drag.

To convey an idea on the turbulence fluctuations, figure 4 shows a configuration of the instantaneous streamwise velocity in the reference REF case and case L80. Panels A and B show a longitudinal  $x - y$  section whilst panels C and D show the transverse  $y - z$  plane at the tip of the bump with a magnification near the bump wall in the inset. The instantaneous fields in the longitudinal section confirm that the separation region seen in the reference case, panel A, almost disappears in the superhydrophobic case, panel B. In the transverse  $y - z$  plane, the effect of the SHS, in an alternating zero/finite velocity at the bottom wall, results in modified turbulence structure at the wall, panel D.

As anticipated, the decrease of the recirculation bubble dimension is induced by the increase of the turbulent velocity fluctuations. The analysis can be made quantitative by considering the turbulent kinetic energy (TKE) equation,

$$\frac{\partial \Phi_j}{\partial x_j} = -\varepsilon + \Pi + \left\langle \frac{\Delta p'}{L_x} u'_x \right\rangle \quad (6)$$

where  $\varepsilon = \langle 1/\text{Re}(\partial u'_i/\partial x_j)(\partial u'_i/\partial x_j) \rangle$  is the TKE pseudo-dissipation rate,  $\Pi = \langle u'_i u'_j \rangle \partial U_i / \partial x_j$  is the production of TKE,  $\langle \Delta p' u'_x / L_x \rangle$  is the external source of energy due to the fluctuating part of the pressure gradient-velocity correlation, and  $\Phi_j$  is the spatial flux contributing zero net

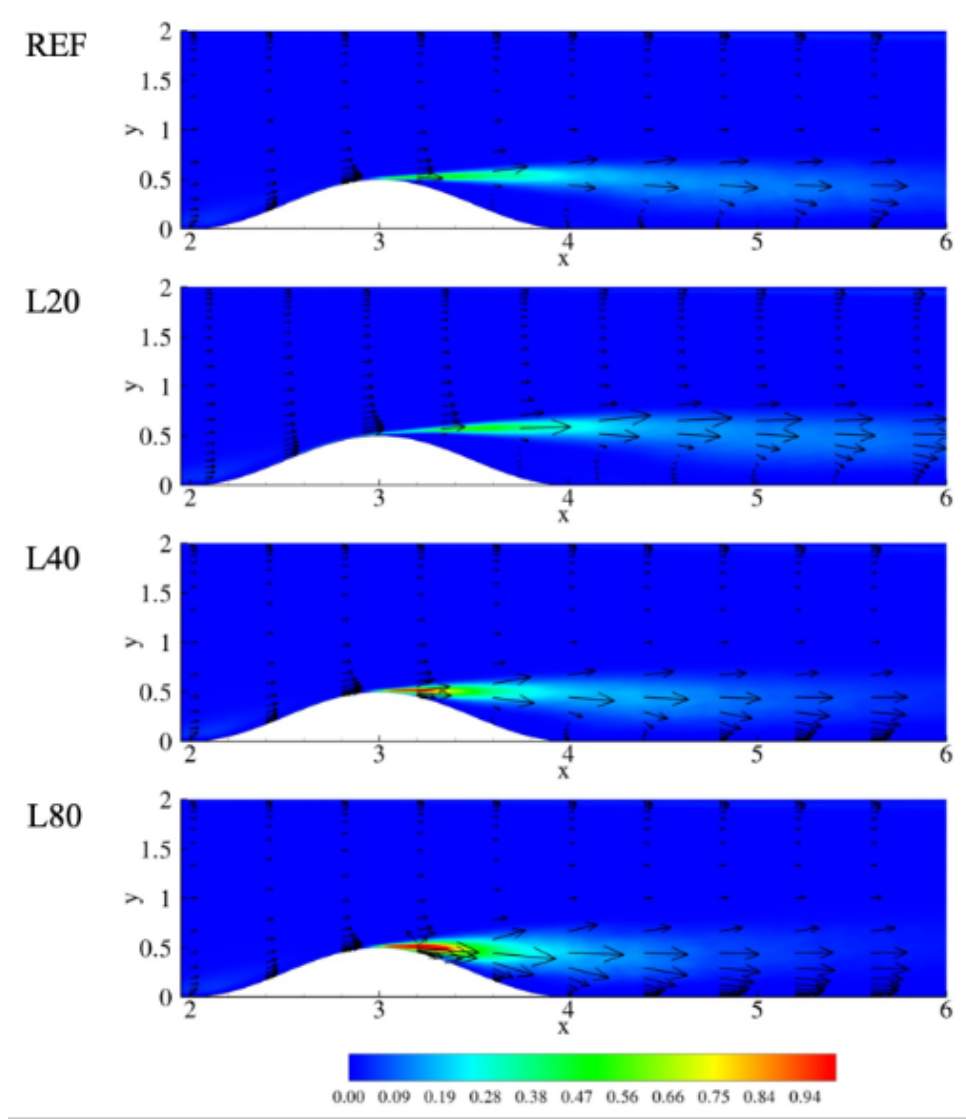


Figure 5. Turbulent kinetic energy production  $\Pi$  as background colour and spatial energy flux  $\Phi_j$  as vectors.

power when integrated over the whole domain given by

$$\Phi_j = U_j k + \frac{1}{2} \langle u'_i u'_i u'_j \rangle + \langle p' u'_j \rangle - \frac{1}{\text{Re}} \frac{\partial k}{\partial x_j} \quad (7)$$

where  $k = 1/2 \langle u'_i u'_i \rangle$  is the turbulent kinetic energy. The energy provided by the fluctuations of inlet/outlet pressure drop is negligible with respect to the other source term,  $\Pi$ , i.e.  $\langle \Delta p' u'_x / L_x \rangle \simeq 10^{-5} \Pi$ .

Figure 5 reports the production term  $\Pi$  (background colour) and the energy spatial fluxes  $\vec{\Phi}$  (vectors) for the different cases considered in the manuscript. The production term increases when the periodicity length increases since the superhydrophobic surfaces produce higher velocity fluctuations with respect to the classical no-slip wall, as previously discussed. Whilst this increase of velocity fluctuations would produce an increase of the friction drag, overwhelmed by the fluid slip at the wall, it produces a sensible decrease of the form drag by delaying the



separation. The production term feeds the flow close to the bump wall<sup>37,38</sup> with additional energy with respect to the reference case resulting in a delayed separation point and a smaller recirculation bubble.

#### **IV. CONCLUSIONS**

Superhydrophobic surfaces (SHS) reduce the form drag by reducing the separation bubble behind a bluff body in turbulent flow. The separation point is delayed whilst the reattachment point is anticipated, corresponding to a decrease of the separation bubble dimensions of up to 35%. The culprit of this phenomenon is the substantial modification of the turbulent kinetic energy production mechanisms induced by the superhydrophobic surface. The turbulent kinetic energy production increases in the shear layer, and spatial fluxes are able to sustain a higher level of turbulent fluctuations near the wall. It follows that the resulting flow can withstand more effectively the adverse pressure gradient delaying the separation point, reducing the dimensions of the separation bubble and facilitating pressure recovery in the reattachment region. In the present analysis, the main assumption is that the gas entrapped in the SHSs asperities is stable and no liquid infusion in these asperities occurs. We also assume a non-deformable interface, which might be sometimes different from reality. Dedicated experimental studies are needed to address the conditions at which the gaseous bubbles stably remain in the asperities and the interface can be assumed stable or not.

#### **AUTHOR'S CONTRIBUTION**

All authors contributed equally to this work.

#### **ACKNOWLEDGEMENTS**

We acknowledge the CINECA award under the ISCRA initiative, for the availability of high performance computing resources.

#### **DATA AVAILABILITY**

The data that support the findings of this study are available from the corresponding author upon reasonable request.

#### **REFERENCES**

- <sup>1</sup>L. Landau and E. Lifshitz, "Fluid mechanics: Course of theoretical physics. vol. 6 butterworth," (1987).
- <sup>2</sup>G. Batchelor, *An introduction to fluid dynamics* (Cambridge University Press, 2000).
- <sup>3</sup>U. Frisch, *Turbulence: the legacy of AN Kolmogorov* (Cambridge university press, 1995).

- <sup>4</sup>Y. Kametani, K. Fukagata, R. Örlü, and P. Schlatter, “Effect of uniform blowing/suction in a turbulent boundary layer at moderate reynolds number,” *International Journal of Heat and Fluid Flow* **55**, 132–142 (2015).
- <sup>5</sup>N. Beck, T. Landa, A. Seitz, L. Boermans, Y. Liu, and R. Radespiel, “Drag reduction by laminar flow control,” *Energies* **11**, 252 (2018).
- <sup>6</sup>B. R. Elbing, S. Mäkiharju, A. Wiggins, M. Perlin, D. R. Dowling, and S. L. Ceccio, “On the scaling of air layer drag reduction,” *Journal of fluid mechanics* **717**, 484–513 (2013).
- <sup>7</sup>P. Spalart, M. Strelets, and A. Travin, “Direct numerical simulation of large-eddy-break-up devices in a boundary layer,” *International Journal of Heat and Fluid Flow* **27**, 902–910 (2006).
- <sup>8</sup>B. Mele, L. Russo, and R. Tognaccini, “Drag bookkeeping on an aircraft with riblets and nlf control,” *Aerospace Science and Technology* **98**, 105714 (2020).
- <sup>9</sup>W. Li, W. Jessen, D. Roggenkamp, M. Klaas, W. Silex, M. Schiek, and W. Schröder, “Turbulent drag reduction by spanwise traveling ribbed surface waves,” *European Journal of Mechanics-B/Fluids* **53**, 101–112 (2015).
- <sup>10</sup>J. P. Rothstein, “Slip on superhydrophobic surfaces,” *Annual Review of Fluid Mechanics* **42**, 89–109 (2010).
- <sup>11</sup>F. Schellenberger, N. Encinas, D. Vollmer, and H.-J. Butt, “How water advances on superhydrophobic surfaces,” *Physical review letters* **116**, 096101 (2016).
- <sup>12</sup>M. Fu, I. Arenas, S. Leonardi, and M. Hultmark, “Liquid-infused surfaces as a passive method of turbulent drag reduction,” *Journal of Fluid Mechanics* **824**, 688 (2017).
- <sup>13</sup>A. Rastegari and R. Akhavan, “On drag reduction scaling and sustainability bounds of superhydrophobic surfaces in high reynolds number turbulent flows,” *Journal of Fluid Mechanics* **864**, 327–347 (2019).
- <sup>14</sup>H. Park, H. Park, and J. Kim, “A numerical study of the effects of superhydrophobic surface on skin-friction drag in turbulent channel flow,” *Physics of Fluids* **25**, 110815 (2013).
- <sup>15</sup>H. Park, G. Sun, *et al.*, “Superhydrophobic turbulent drag reduction as a function of surface grating parameters,” *Journal of Fluid Mechanics* **747**, 722–734 (2014).
- <sup>16</sup>T. Min and J. Kim, “Effects of hydrophobic surface on skin-friction drag,” *Physics of Fluids* **16**, L55–L58 (2004).
- <sup>17</sup>A. Rastegari and R. Akhavan, “On the mechanism of turbulent drag reduction with superhydrophobic surfaces,” *Journal of Fluid Mechanics* **773** (2015).
- <sup>18</sup>C. Lee, C.-H. Choi, and C.-J. Kim, “Superhydrophobic drag reduction in laminar flows: A critical review,” *Experiments in Fluids* **57**, 176 (2016).
- <sup>19</sup>B. R. Gruncell, N. D. Sandham, and G. McHale, “Simulations of laminar flow past a superhydrophobic sphere with drag reduction and separation delay,” *Physics of Fluids* **25**, 043601 (2013).
- <sup>20</sup>R. J. Daniello, N. E. Waterhouse, and J. P. Rothstein, “Drag reduction in turbulent flows over superhydrophobic surfaces,” *Physics of Fluids* **21**, 085103 (2009).
- <sup>21</sup>E. Aljallis, M. A. Sarshar, R. Datla, V. Sikka, A. Jones, and C.-H. Choi, “Experimental study of skin friction drag reduction on superhydrophobic flat plates in high reynolds number boundary layer flow,” *Physics of fluids* **25**, 025103 (2013).
- <sup>22</sup>T. Jelly, S. Jung, and T. Zaki, “Turbulence and skin friction modification in channel flow with streamwise-aligned superhydrophobic surface texture,” *Physics of Fluids* **26**, 095102 (2014).

- <sup>23</sup>S. Srinivasan, J. A. Kleingartner, J. B. Gilbert, R. E. Cohen, A. J. Milne, and G. H. McKinley, “Sustainable drag reduction in turbulent taylor-couette flows by depositing sprayable superhydrophobic surfaces,” *Physical review letters* **114**, 014501 (2015).
- <sup>24</sup>R. Costantini, J.-P. Mollicone, and F. Battista, “Drag reduction induced by superhydrophobic surfaces in turbulent pipe flow,” *Physics of Fluids* **30**, 025102 (2018).
- <sup>25</sup>H. Choi, J. Lee, and H. Park, “Wake structures behind a rotor with superhydrophobic-coated blades at low reynolds number,” *Physics of Fluids* **31**, 015102 (2019).
- <sup>26</sup>S. Wang, K. Liu, X. Yao, and L. Jiang, “Bioinspired surfaces with superwettability: new insight on theory, design, and applications,” *Chemical reviews* **115**, 8230–8293 (2015).
- <sup>27</sup>S. Türk, G. Daschiel, A. Stroh, Y. Hasegawa, and B. Frohnäpfel, “Turbulent flow over superhydrophobic surfaces with streamwise grooves,” *Journal of Fluid Mechanics* **747**, 186–217 (2014).
- <sup>28</sup>H. Hu, J. Wen, L. Bao, L. Jia, D. Song, B. Song, G. Pan, M. Scaraggi, D. Dini, Q. Xue, *et al.*, “Significant and stable drag reduction with air rings confined by alternated superhydrophobic and hydrophilic strips,” *Science advances* **3**, e1603288 (2017).
- <sup>29</sup>A. Rajappan, K. Golovin, B. Tobelmann, V. Pillutla, Abhijeet, W. Choi, A. Tuteja, and G. H. McKinley, “Influence of textural statistics on drag reduction by scalable, randomly rough superhydrophobic surfaces in turbulent flow,” *Physics of Fluids* **31**, 042107 (2019).
- <sup>30</sup>H. J. Im and J. H. Lee, “Comparison of superhydrophobic drag reduction between turbulent pipe and channel flows,” *Physics of Fluids* **29**, 095101 (2017).
- <sup>31</sup>J. Lee, H. Kim, and H. Park, “Effects of superhydrophobic surfaces on the flow around an naca0012 hydrofoil at low reynolds numbers,” *Experiments in Fluids* **59**, 111 (2018).
- <sup>32</sup>Y. Xiong and D. Yang, “Influence of slip on the three-dimensional instability of flow past an elongated superhydrophobic bluff body,” *Journal of Fluid Mechanics* **814**, 69–94 (2017).
- <sup>33</sup>P. Moin and J. Kim, “Tackling turbulence with supercomputers,” *Scientific American* **276**, 62–68 (1997).
- <sup>34</sup>F. Stella, N. Mazellier, and A. Kourta, “Scaling of separated shear layers: an investigation of mass entrainment,” *Journal of Fluid Mechanics* **826**, 851–887 (2017).
- <sup>35</sup>B. Krank, M. Kronbichler, and W. A. Wall, “Direct numerical simulation of flow over periodic hills up to  $Re_h=10595$ ,” *Flow, Turbulence and Combustion*, 1–31 (2017).
- <sup>36</sup>L. A. C. A. Schiavo, W. R. Wolf, and J. L. F. Azevedo, “Turbulent kinetic energy budgets in wall bounded flows with pressure gradients and separation,” *Physics of Fluids* **29**, 115108 (2017).
- <sup>37</sup>J.-P. Mollicone, F. Battista, P. Gualtieri, and C. Casciola, “Turbulence dynamics in separated flows: The generalised kolmogorov equation for inhomogeneous anisotropic conditions,” *Journal of Fluid Mechanics* **841**, 1012–1039 (2018).
- <sup>38</sup>J.-P. Mollicone, F. Battista, P. Gualtieri, and C. M. Casciola, “Effect of geometry and reynolds number on the turbulent separated flow behind a bulge in a channel,” *Journal of Fluid Mechanics* **823**, 100–133 (2017).
- <sup>39</sup>P.-Y. Passaggia and U. Ehrenstein, “Optimal control of a separated boundary-layer flow over a bump,” *Journal of Fluid Mechanics* **840**, 238–265 (2018).
- <sup>40</sup>C. Kähler, S. Scharnowski, and C. Cierpka, “Highly resolved experimental results of the separated flow in a channel with streamwise periodic constrictions,” *Journal of Fluid Mechanics* **796**, 257–284 (2016).

- <sup>41</sup>R. Matai and P. Durbin, “Large-eddy simulation of turbulent flow over a parametric set of bumps,” *Journal of Fluid Mechanics* **866**, 503–525 (2019).
- <sup>42</sup>F. Fadla, F. Alizard, L. Keirsbulck, J.-C. Robinet, J.-P. Laval, J.-M. Foucaut, C. Chovet, and M. Lippert, “Investigation of the dynamics in separated turbulent flow,” *European Journal of Mechanics-B/Fluids* (2019).
- <sup>43</sup>P. Fischer, J. W. Lottes, and S. G. Kerkemeier, “Nek5000 - Open source spectral element CFD solver. Argonne National Laboratory, Mathematics and Computer Science Division, Argonne, IL, see <http://nek5000.mcs.anl.gov>,” (2008).
- <sup>44</sup>A. T. Patera, “A spectral element method for fluid dynamics: laminar flow in a channel expansion,” *Journal of computational Physics* **54**, 468–488 (1984).
- <sup>45</sup>M. Liravi, H. Pakzad, A. Moosavi, and A. Nouri-Borujerdi, “A comprehensive review on recent advances in superhydrophobic surfaces and their applications for drag reduction,” *Progress in Organic Coatings* **140**, 105537 (2020).